Journal of Physical Science Vol. 36(2), 81–97, 2025



Characteristics of Zn_xNi_{1-x}O Nano-Powder Composites Produced via Chemical Co-Precipitation: Structural and Optical

Mohammed A. Abed,1* R. S. Mohammed,2 Raghad T. Ahmed,2 Mehdi H. Diwan2

¹Diyala Directorate General of Education, 32001 Ba'aqubah, Diyala, Iraq ²Physics Department, College of Science, Diyala University, 32001 Ba'aqubah, Diyala, Iraq

*Corresponding author: mohammad8888985@yahoo.com

Published online: 29 August 2025

To cite this article: Abed, M. A. et al. (2025). Characteristics of $Zn_xNi_{1-x}O$ nano-powder composites produced via chemical co-precipitation: Structural and optical. *J. Phys. Sci.*, 36(2), 81–97. https://doi.org/10.21315/jps2025.36.2.5

To link this article: https://doi.org/10.21315/jps2025.36.2.5

ABSTRACT: Chemical co-precipitation was applied to create $Zn_xNi_{1-x}O$ nano-powder material composites. This was achieved by mixing varied ratios (X = 0.0, 0.25, 0.50, 0.75 and 1.0) of zinc oxide (ZnO) and nickel oxide (NiO). The fabricated samples were then annealed at 400°C for 2 h. The outcomes of the X-ray diffraction (XRD) analysis revealed hexagonal or cubic lattices. The crystallite sizes were evaluated using Debye-Scherrer and Williamson-Hall equations. The outcomes of the Fourier transform infrared (FTIR) spectroscopy verified the existence of ZnO and NiO in all samples. The results of the field emission scanning electron microscopy (FESEM) revealed different nano-structures, and the morphology relied on the X. The outcomes of the energy-dispersive X-ray (EDX) confirmed the purity of the samples. Moreover, zinc (Zn), nickel (Ni) and oxygen (O) were discovered, which are compatible with the XRD and FTIR outcomes. Finally, the Kubelka-Munk function (F[R ∞]) was applied to evaluate the samples' optical characteristics in the ultraviolet-visible (UV-Vis) range. The energy gap (Eg) of the samples varied according to the X. Numerous samples had two Eg.

Keywords: $Zn_xNi_{1-x}O$, co-precipitation, composites, nano-powders, nickel oxide, zinc oxide, Kubelka-Munk, Williamson-Hall

1. INTRODUCTION

Nickel oxide (NiO) is a *p*-type metal oxide and a transition semiconductor. It is a promising substitute for graphite due to its unique physical and chemical characteristics. In addition, it has a wide band gap (1.2 eV–4.0 eV), cost-effectiveness, and outstanding chemical and thermal stability. ¹⁻³ Recent achievements have seen the function of NiO nanoparticles (NPs) for numerous purposes. This involves gas detectors, solar panels, supercapacitors, fuel cells, photovoltaic devices, electrochemical smart windows and catalysts. ¹ Various techniques have been employed to synthesise NiO thin nano-films and nano-powders. There are various methods, including solution spray pyrolysis,

sol-gel, co-deposition and hydrothermal methods. Of these methods, co-deposition stands out due to its affordability, simplicity, size control, rapid preparation and facility to create extremely homogenous materials.² Zinc oxide (ZnO), on the other hand, is a transparent conductive oxide that has semiconductor specifications and a band gap of ±3.3 Ev. Mixing both these oxides into a nano-composite may develop photocatalytic and optoelectronic effectiveness. Additionally, mixing metals into oxide matrices may yield novel materials with outstanding specifications for diverse functions. Both NiO and ZnO are widely used in semiconductor and chemical manufacturing, primarily in catalytic, adsorption, de-hydrogenation, and drying processes. For example, Panigrahi et al. used a hydrated chemical method to synthesise a Ni_{1-x}Zn_xO/Ni nano-composite with a spherical lattice.⁶ Meanwhile, Ahmed et al. used chemical co-precipitation to generate a cubic Ni_{1-v}Zn_vO nano-composite that primarily contained NiO.² As such, this present study fabricated Zn_xNi_{1-x}O nano-composites by mixing zinc cations (Zn²⁺) into a NiO lattice. Chemical co-precipitation was utilised as it is cost-effective and efficient. The structural and optical properties of the outgoing composites were then analysed to estimate the influence of Zn²⁺ incorporation.

2. MATERIALS AND PROCEDURES

2.1 Materials

The next items were obtained from Thomas Baker (Chemicals) Pvt. Ltd., Mumbai, India:

- a. Pure ethanol (C₂H₆O)
- b. Distilled water
- c. High-purity hexahydrates of zinc nitrate $(Zn(NO_3)_2 \cdot 6H_2O)$
- d. Nickel nitrate (Ni(NO₃)₂·6H₂O)
- e. Ammonium hydroxide (NH₄OH)

2.2 The Synthesis of Zn_xNi_{1-x}O Nano-Powders

Chemical co-precipitation was used to manufacture the $Zn_xNi_{1-x}O$ nano-powder composites.⁷ This was achieved by mixing varying ratios (X) of Zn into a NiO lattice. The X were 0.0, 0.25, 0.50, 0.75 and 1.0. When X = 0.0, the sample was pure NiO. When X = 1.0, the sample was ZnO. A magnetic stirrer was used to dissolve 0.01 mL of $Zn(NO_3)_2.6H_2O$ and $Ni(NO_3)_2.6H_2O$ in 100 mL of distilled water. The magnetic stirrer was set at 60°C. An alkaline solution of 0.1 M NH_4OH was added drop by drop to the mixed solution employing a burette. It is frequently mixed at 60°C for

1 h to certify homogeneity. The powder was washed and filtered using filter paper and distilled water to remove any remaining insoluble nitrate, followed by 48 h of drying at 60°C in a convection oven. The dried powder was ground with a ceramic mortar to produce extremely fine particles. Finally, the powder particles were sintered at 400°C in an electric convection oven for a couple of hours before being gradually cooled in a combustion chamber for 24 h. As a result, the powder produced was appropriate for examination.

2.3 Characterising the Zn_xNi_{1-x}O Nano-Powder Composites

A BrukerTM D8 Advance, X-ray diffraction (XRD) was utilised to investigate the structure of the nano-composite powder (Karlsruhe, Germany). It was run at 40 kV and 60 mA, applying copper K-alpha (Cu K-α) radiation (λ = 1.5404 Å) on the target material within two-theta (2θ) scanning range of 20°–80°. An ABB™ MB 3000 Fourier transform infrared (FTIR) spectrometer was employed to detect the samples' functional groups (Québec, Canada). It was prepared with horizontal minimised attenuated total reflectance (ATR) and could be measured within 4,000 cm⁻¹–400 cm⁻¹ at room temperature. Following that, a NovaTM NanoSEM 450 field emission scanning electron microscope (FESEM) was employed to observe the morphology of the samples (Brno, Czech Republic). Besides that, a TESCAN™ energy dispersive X-ray (EDX) analyser was applied to verify their chemical compositions (Brno, Czech Republic). Finally, a ShimadzuTM UV-1800 ultravioletvisible (UV-Vis) spectrometer was applied to evaluate the samples' optical UV-Vis properties (Kyoto, Japan). In this measuring, the extent was 200 nm–800 nm and was done at room temperature.

3. RESULTS AND DISCUSSION

3.1 XRD Patterns

Figure 1 displays the XRD patterns of the samples. For indication, the standard patterns of pure oxide cards (ICCD), really ZnO #00-2107059 and NiO #00-432-9325, were involved. The characteristic peaks revealed at $2\theta = 31.81^{\circ}$, 34.47° and 36.3° in the pure ZnO (X = 1.0) sample matched the crystal planes (100), (002) and (101), respectively, verifying the formation of hexagonal lattices, which aligned with the products of Rambu et al.⁸ Alternatively, the characteristic peaks observed at $2\theta = 37.18^{\circ}$, 43.23° and 62.83° in the pure NiO (X = 0.0) sample agree with the crystal planes (111), (200) and (220), respectively, denoting the composition of cubic lattices, in line with the results achieved by Hameed et al.⁹

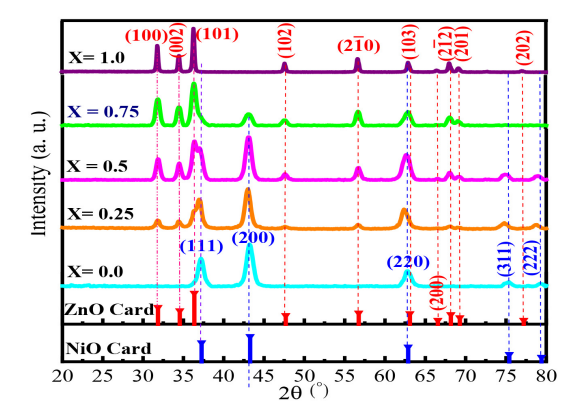


Figure 1: The X-ray patterns of the samples, with ZnO #00-210-7059 and NiO #00-432-9325 ICCD cards for comparison.

As observed in Figure 1 and Table 1, the XRD patterns of the mixed samples (X = 0.25, 0.50 and 0.75) displayed distinct peaks conforming to ZnO and NiO. These patterns exhibited no secondary phases and corresponded well with the ICCD cards. As the X increased, the peaks regularly shifted towards those of ZnO. This was mainly actually in the mixed (X = 0.75) sample. More explicitly, its full width at half maximum (FWHM) diminished, and its peaks shifted in the (101) direction towards ZnO's preferred peak. The primary and preferred peak of the cubic-latticed NiO conformed to the preferred (200) direction in the mixed (X = 0.25 and 0.50) samples. This denotes that the Zn²⁺ and Ni²⁺ had been successfully combined into the NiO lattice. Furthermore, the shift in the preferred growth direction could be because of the influence of the high material concentration on the sample's surface structure. In

The Debye-Scherrer formula (Equation 1) was utilised to establish the average crystalline sizes ($D_{(av)}$) of the samples.¹² The $D_{(av)}$ of the mixed (X = 0.75) and the pure ZnO (X = 1.0) samples were defined at the preferred crystal plane (101). The $D_{(av)}$ of the pure NiO (X = 0.0) and mixed (X = 0.25 and 0.50) samples were estimated at the preferred and preferred crystal plane (200).

$$D_{(av)} = (k \lambda / \beta \cos \theta) \tag{1}$$

Where λ is the incident X-ray wavelength (0.154 nm), θ is the diffraction angle, and k = 0.98 is the shape factor. For β , the FWHM of the strongest diffraction peak is shown. The calculation revealed that, as the X of Zn^{2+} in the NiO lattice increased, the $D_{(av)}$ of the NiO lattice increased. The $D_{(av)}$ increased as the amount of Zn^{2+} increased due to the replacement of more Ni⁺ on the surface, which accelerated its growth via crystallisation, which is the force of attraction between the NPs.

However, the $D_{(av)}$ decreased very slightly in the mixed (X = 0.50) sample due to the distortion of the Zn^{2+} , wherein additional defects were inserted into the crystal lattice structure. ^{10,13} (see Table 1).

Table 1: The XRD outcomes of the structural characteristics of the $Zn_xNi_{1-x}O$ nano-composites.

Parameters	0.0(200)	0.25(200)	0.50(200)	0.75(101)	1.0(101)
2θ (°)	43.2300	42.9800	43.0800	36.3300	36.3000
FWHM (deg)	0.9928	0.8751	0.8891	0.8036	0.2622
d (Å)	2.0911	2.1026	2.0980	2.4708	2.4728
D(av) nm Scherrer	8.6100	9.7600	9.6100	10.4100	31.9000
D(aV) nm W-H	6.9700	8.2800	12.4400	11.0800	44.7000
Dislocation density (δ) (nm ⁻²)	1.35×10^{-2}	1.05×10^{-2}	1.08×10^{-2}	9.23×10^{-3}	9.83 × 10 ⁻⁴
Microstrain (ε)	4.03×10^{-3}	3.55×10^{-3}	3.61×10^{-3}	3.33×10^{-3}	1.09×10^{-3}

As seen in Equation 2, the Williamson-Hall formula was also used to calculate the $D_{(av)}$ of all the samples.¹⁴

$$\beta \cos \theta = (k \lambda / D) + 4 \varepsilon \sin \theta \tag{2}$$

Where ε is the lattice stress of the crystals. The peak width was used as a function of 2θ to execute the Williamson-Hall formula, which accounts for variations in the stress and volume. To estimate the $D_{(av)}$ and ε of the samples, the β cos θ was plotted on the Y-axis vs $4 \sin \theta$ on the X-axis (Figure 2). The Williamson-Hall graphs showed linear fits for the samples. Calculating the ε and $D_{(av)}$ involved using the slope and intercept. The Williamson-Hall plots and the Debye-Scherer correlations were used to compare the $D_{(av)}$ (Figure 3, Table 1). The stresses and defects that the entry of the Zn⁺ into the NiO lattice caused resulted in minor differences in the $D_{(av)}$. However, the $D_{(av)}$ behaviour appeared to be largely consistent with the Debye-Scherer correlations.

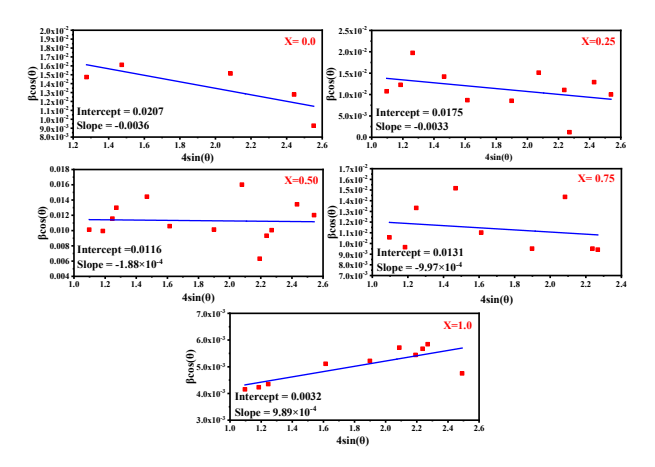


Figure 2: The plots of the estimated samples using the Williamson-Hall formula.

A negative slope, indicating compressive stress, was observed in the pure NiO (X = 0.0) sample and the mixed (X = 0.25) sample (Figure 2). Meanwhile, a positive slope, indicating tensile stress, was observed in the mixed (X = 0.50 and 0.75) samples and the pure ZnO (X = 1.0) sample. This could be attributed to the higher levels of Zn²⁺ in the mixed (X = 0.50 and 0.75) samples and the pure ZnO (X = 1.0) sample, which caused the stress to shift from compressive to tensile. At smaller $D_{(av)}$, more energy is required to integrate Zn²⁺ into the NiO lattice, which would inhibit the crystallisation process and reduce the $D_{(av)}$.¹⁵

Equations 3 and 4 were used to ascertain the microstrain (ϵ) and dislocation density (δ) of the samples:^{17, 14}

$$\varepsilon = \beta \cos \theta / 4 \tag{3}$$

$$\delta = 1/D^2 \tag{4}$$

A low δ indicates good crystallisation in a nanomaterial. Furthermore, as the δ is proportional to the $D_{(av)}$, it significantly affects the crystalline characteristics of the material. In the present study, the $D_{(av)}$ affected the overall stress in the samples. However, the δ depended on the amount of ZnO. More specifically, as the $D_{(av)}$ increased or decreased, the number of dislocation lines per unit area observed in the samples varied. This is somewhat consistent with the findings of Zeid et al. In the samples varied.

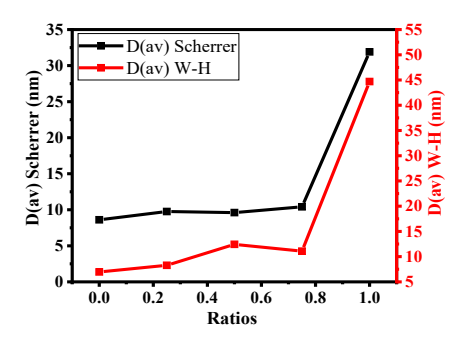


Figure 3: A comparison of the D(av) of the samples using the Debye-Scherrer and Williamson-Hall formulas.

Equations 5 and 6 used the extremely intense preferred crystal planes (101) and (002) of the hexagonal lattice and the crystal plane (200) of the cubic lattice to determine that a, b and c were the lattice parameters of both the lattice systems. Table 2 presents the results.

$$1/d^{2}_{(hkl)} = 4/3 (h^{2} + hk + k^{2}/\alpha^{2}) + (l^{2}/c^{2})$$
(5)

$$\alpha = d(h^2 + k^2 + l^2)^{1/2} \tag{6}$$

Meanwhile, Equations 7 and 8 were utilised to estimate the volume of the unit cell in the hexagonal and cubic lattices (Table 2):^{10,20}

$$V = 0.866 \times a^2 \times c \tag{7}$$

$$V = \alpha^3 \tag{8}$$

As seen in Table 2, the lattice parameters of the samples changed. More specifically, the lattice parameters of the mixed (X = 0.25, 0.50 and 0.75) samples increased more than those of the pure (X = 0.0 and 1.0) samples. This could be attributed to Zn^{2+} replacing the Ni²⁺ in the NiO lattice, which causes a slight dispersion in the crystal lattice due to the difference in their Shannon ion diameters (0.060 nm vs 0.055 nm). This theory is also supported by the slight increase observed in the unit cell volumes of the mixed (X = 0.25, 0.50 and 0.75) samples compared to that of the pure (X = 0.0 and 1.0) samples (Table 2). This finding has been corroborated by previous studies. 11,21

Ratios	Crystallite size D(Scherrer) (nm)	Lattice parameter a (Å)	Lattice parameter c (Å)	Volume (ų)
0.00	8.61	4.1827	4.1827	73.1796
0.25	9.76	4.2052	4.2052	74.3635
0.50	9.61	4.1960	4.1960	73.8765
0.75	10.41	3.2478	5.2044	47.5432
1.00	31.90	3.2464	5.2008	47.4716

Table 2: The Debye-Scherrer-based $D_{(av)}$, lattice constants, and unit cell volumes of the samples.

3.2 FTIR Spectra

Figure 4 shows the results of the FTIR analysis. As seen, the absorption bands of the samples ranged between 3,421 cm⁻¹–3,475 cm⁻¹ due to the O-H bond vibrations associated with the presence of water.²²

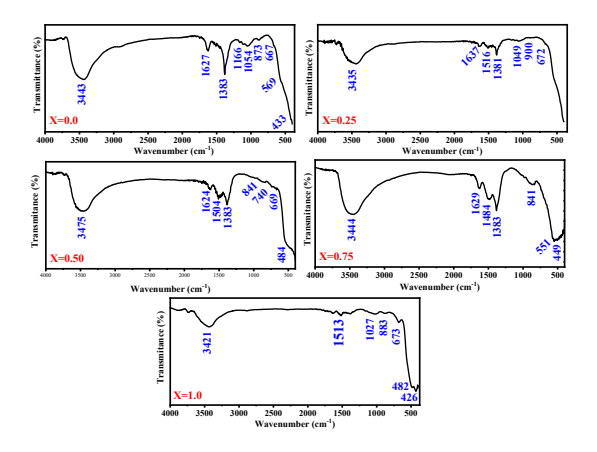


Figure 4: The FTIR spectra of the samples.

The band observed at 1,166 cm⁻¹ indicates the vibrations of the C-O bonds in the pure NiO (X = 0.0) sample.³ A weak band was visible in the O-H bond vibrations of the hydroxyl group at roughly 1,625 cm⁻¹.²⁰ Furthermore, repeated washing did not remove the NO₃⁻, whose presence is confirmed by the band observed at ~1,383 cm⁻¹.¹⁰ The N-O bond vibrations caused the band observed at ~1,513 cm⁻¹, while the vibrations of the C-N bonds caused the band observed at 1,484 cm⁻¹. The band observed at ~1,054 cm⁻¹ represents the stretching vibrations of the C-N bonds, while the band observed at 1,027 cm⁻¹ represents the vibrations of the C-O bonds in amino acids. Lastly, the bands observed at ~844 cm⁻¹ and 883 cm⁻¹ indicate the vibrations of the C-H bonds. This is consistent with the results of other studies.^{23–26}

It is important to note that the frequency range of the metal oxide bonds was below the vibrational range of 1,000 cm⁻¹, and some peaks in the FTIR vibrations shifted in a direction that indicated increased oxide concentrations. The bands observed at ~667 cm⁻¹, ~433 cm⁻¹ and ~569 cm⁻¹ indicate the presence of NiO, but the bands observed at ~426 cm⁻¹, ~482 cm⁻¹, ~673 cm⁻¹ and ~740 cm⁻¹ indicate the presence of ZnO. $^{9,20,22,27-30}$ In the pure (X = 0.0 and 1.0) samples, these results revealed several changes. More specifically, it is possible that the shift in the spectral frequency was caused by the difference in the ionic radii of Zn²⁺ and Ni²⁺, which made it easier for the Zn²⁺ to replace the Ni²⁺. Additionally, this validated the inclusion of Zn²⁺ into the NiO lattice, which conforms with the findings of Elkamel et al. 31

3.3 Field Emission Scanning Electron Microscopy

A FESEM was used to evaluate the surface morphology of the samples, which provides information about the size, shape, and evolution of their NPs.

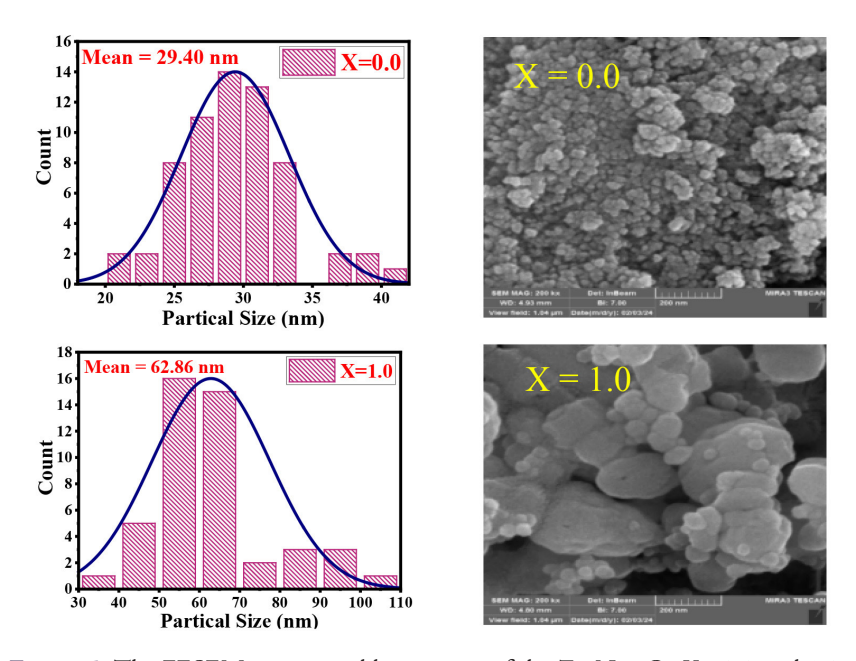


Figure 5: The FESEM images and histograms of the $Zn_xNi_{1-x}O$, X = 0.0 and 1.0.

Figures 5 and 6 show the FESEM images of the samples at 200-kx magnification and 200-nm scale, as well as histograms of their grain sizes, which were measured and drawn using ImageJ and Origin. As seen, the NPs of the pure NiO (X = 0.0) sample easily agglomerated to form irregular spherical lattices with some voids, whereas those of the pure ZnO (X = 1.0) sample did not agglomerate but formed big hexagonal and small spherical lattices with some large voids, in Figure 5.^{20,32}

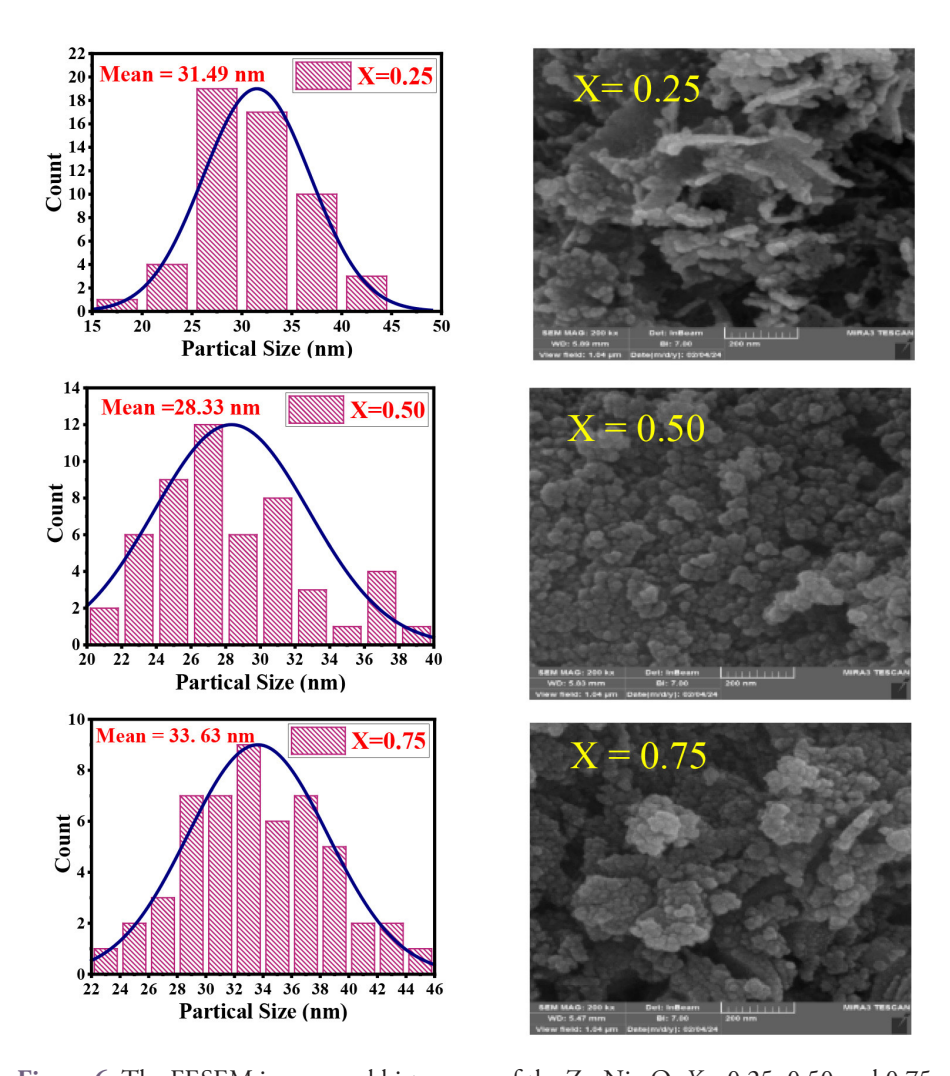


Figure 6: The FESEM images and histograms of the $Zn_xNi_{1-x}O$, X = 0.25, 0.50 and 0.75.

Meanwhile, the NPs of the mixed (X = 0.25, 0.50 and 0.75) samples (see Figure 6) agglomerated and increased as the concentration of Zn^{2+} in the NiO lattice increased. More specifically, irregular voids formed between the NPs, and various forms emerged that changed depending on the X. Furthermore, in the mixed (X = 0.25 and 0.75) samples, the plate-like lattices seemed perpendicular, with an external appearance that was similar to short and long nanowires, which agrees with the observations reported by Raja et al.⁴ The NPs agglomerated due to the attractive forces between them and the tendency of an increase in the surface area-to-volume ratio to reduce the high surface energy, which aligns with the finding of Fabbiyola et al.¹⁰ The grain sizes obtained via FESEM corresponded to the $D_{(av)}$ calculated using the XRD. The grain

sizes of the pure (X = 0.0 and 1.0) samples were ZnO = 62.86 nm and NiO = 29.40 nm, but those of the mixed (X = 0.25, 0.50, and 0.75) samples were 31.49, 28.33 and 33.63 nm, respectively. This indicates that the mixing process was successful, as the X of the Zn²⁺ changed the grain size and shape of the finished NPs.

3.4 EDX Microanalysis

The EDX microanalysis of the pure (X = 0.0 and 1.0) and mixed (X = 0.25, 0.50 and 0.75) samples verified the presence of fundamental elements, such as oxygen (O), Zn and Ni. Figure 7 shows the EDX results of the samples.

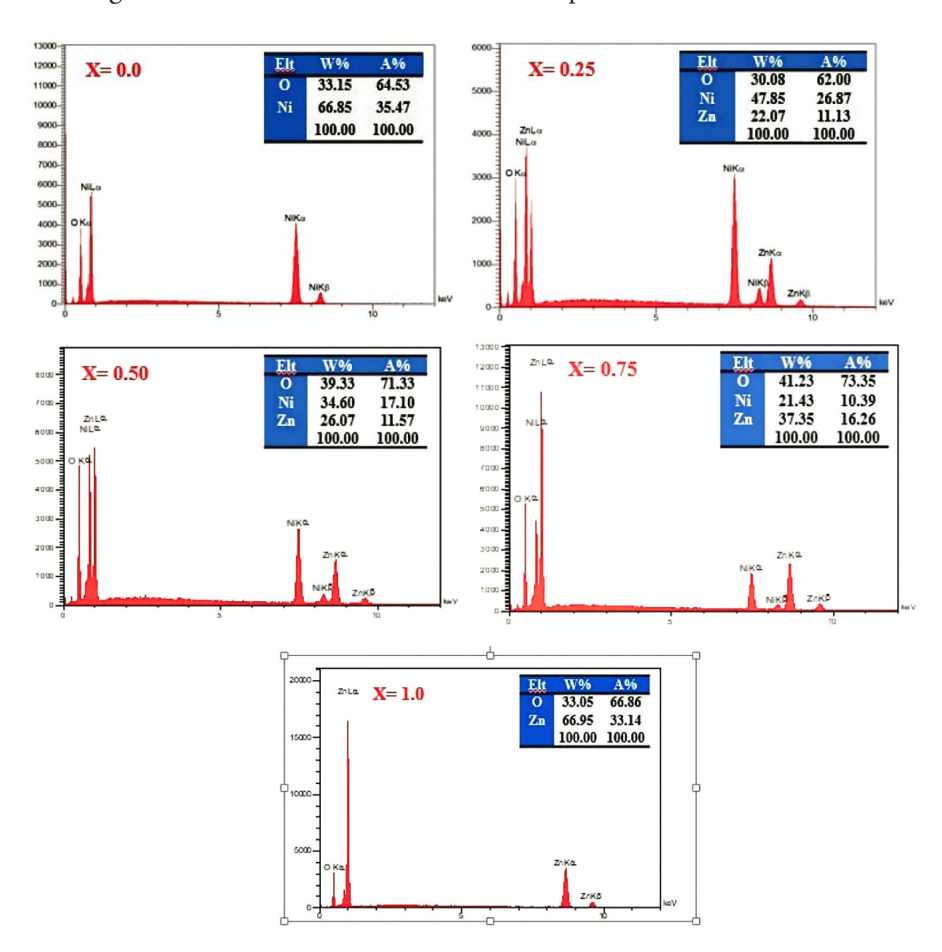


Figure 7: The EDX microanalysis results of the samples.

As seen, all the peaks matched the fundamental constituents of the samples, and no additional unexpected elements were detected, which indicates the purity of the samples at all *X*. Furthermore, a review of the weight ratios of the constituent elements in each sample revealed that the molecular weight (Mt%) and atomic weight (At%) were similar to the weights of the constituent elements during preparation. This indicates that the NPs in the samples, at all *X*, possess robust growth properties.

3.5 UV-Vis Spectroscopy

Absorption spectroscopy, conducted at 200 nm–800 nm, facilitates the efficient and non-destructive investigation of the optical properties of semiconductor NPs.¹⁰ Figure 8 depicts the UV-Vis optical absorption spectrum of the samples.

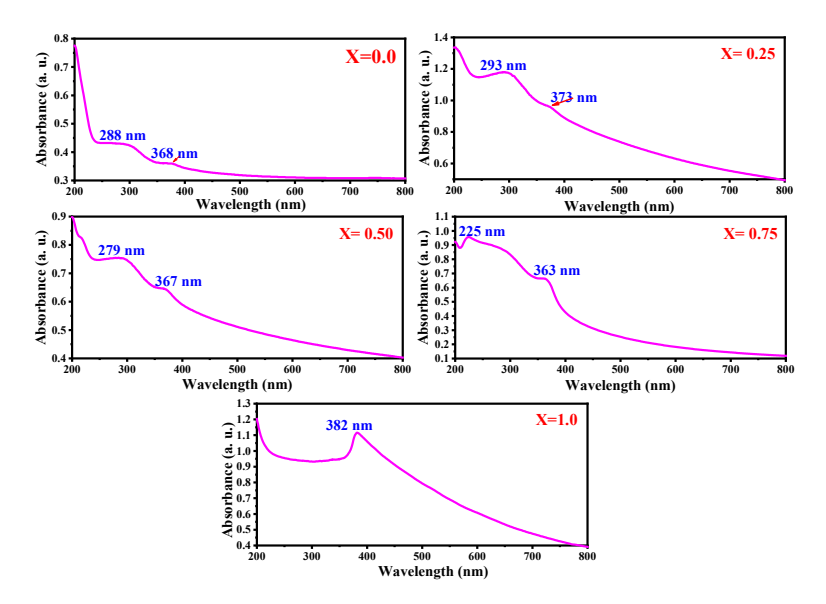


Figure 8: The absorbance spectra as a function of the wavelength of the samples.

The UV-Vis absorption spectra of the samples varied significantly depending on the X. For instance, the peaks observed at 288 nm and 368 nm in the pure NiO (X = 0.0) sample indicate the presence of NiO, while the slight shift that occurred at 293 nm and 373 nm in the mixed (X = 0.25) sample indicates the incorporation of Zn²⁺ into the NiO structure. Apart from that, the peaks observed at 279 nm and 367 nm in the mixed (X = 0.50) sample indicate a significant change in its electronic environment, while the peak observed at 225 nm in the mixed (X = 0.75) sample indicates an electronic structure transition and a dominant phase shift. Lastly, the peak observed at 382 nm in the pure (X = 1.0) sample confirms the presence of ZnO. These changes are consistent with the crystal structures and XRD data reported by previous studies. 4,33,34

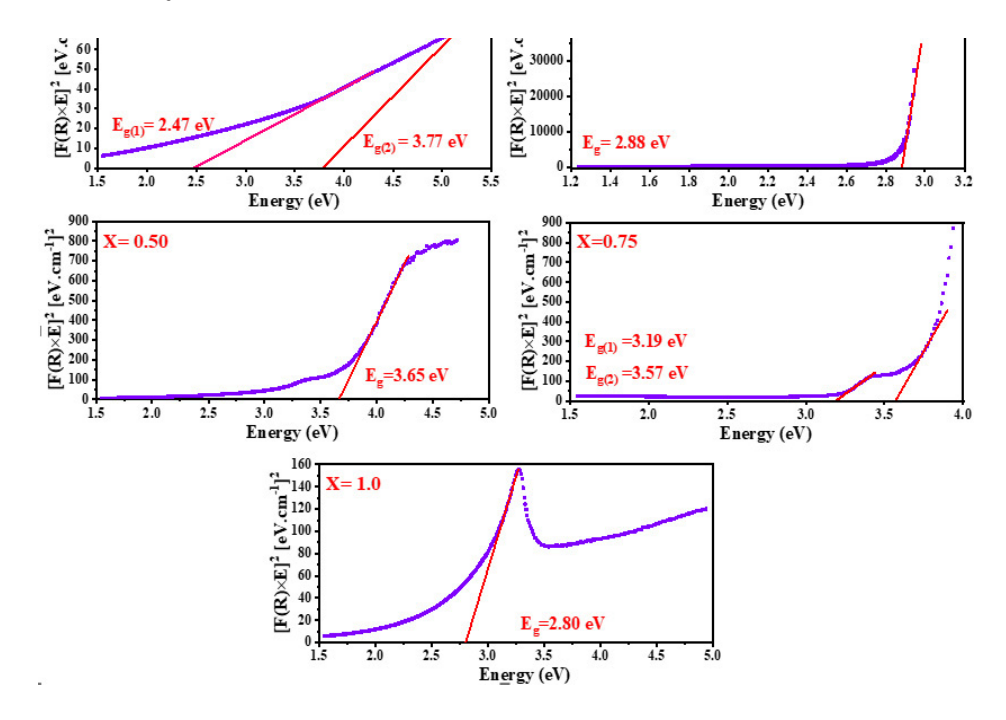


Figure 9: The $F(R\infty)$ plots of the samples.

The optical energy gap (E_g) affects the optical characteristics of absorption. Therefore, the Kubelka-Munk function $(F[R\infty])$ was plotted using the UV-Vis diffuse reflectance (Equation 9):³⁵

$$F(R\infty) = (1-R)^2/2R \tag{9}$$

where $F(R\infty)$ is the Kubelka-Munk function, which was treated as the absorption coefficient, and R is the reflectivity. As seen in Equation 10, the optical band gap was calculated using Tauc's relation.³⁶

$$F(R) hv = A (hv - E_g)^n$$
(10)

where A is the constant, E = hv is the photon energy, and n is the transition probability function. In the event of an indirect band gap, $n = \frac{1}{2}$ was assumed, while for a direct band gap, n = 2 was assumed. Figure 9 displays the $(F[R\infty] hv)^2$ vs. hv plots of all the samples. The linear part of these plots was extrapolated to $(F[R\infty] hv)^2 = 0$ to determine the direct band gap. This is a common process in which the vertical linear curve is extrapolated to intersect the energy axis and determine the energy value of the band gap. The E_g provides insights into the electronic structure of a material and how it changes as the X of Zn^{2+} increases. As seen, two E_g , namely, 2.47 eV and 3.77 eV, were observed in the pure NiO (X = 0.0) sample, indicating

the presence of pure NiO. Furthermore, as X of Zn^{2+} increased, the E_g changed. For instance, the E_g of the mixed (X = 0.25) sample was 2.88 eV, that of the mixed (X = 0.50) sample was 3.65 eV and that of the mixed (X = 0.75) sample was 3.19 eV and 3.57 eV. Meanwhile, the E_g of the pure ZnO (X = 1.0) sample was 2.80 eV, which is consistent with pure ZnO. Therefore, introducing Zn^{2+} into the NiO lattice leads to the substitution of nickel (Ni²⁺) ions, significantly altering the material's electronic structure and E_g . These findings align with the XRD analysis.

The changes in the electronic structure may be attributed to stresses in the crystal lattice due to defects in the structure. It could be due to changes in the carrier density near the conduction band and Fermi level, which leads to an increase in E_g . Fabbiyola et al. arrived at the same conclusion. ¹⁰ Besides that, some of the samples had two E_g due to the existence of impurities and interactions that influenced the crystal lattice structure. According to Li et al., these variables result in the admission of additional energy into the E_g , leading to changes to the physical characteristics of a material. ³⁷

4. CONCLUSION

The present study utilised chemical co-precipitation to fabricate $Zn_xNi_{1-x}O$ nanopowder composites, which included differing X of ZnO and NiO. The outcomes of the XRD analysis revealed a shift in the position of the prominent peak in both the mixed (X = 0.75) and pure ZnO (X = 1.0) sample. However, the FESEM images reveal that agglomeration increased as the X increased. Apart from that, as the EDX results revealed that the Mt% and At% of all the samples were similar to their weights during preparation, it confirmed that the ZnO and NiO had successfully combined. However, the E_g results revealed some variations in the gap values, with some samples having two E_g . This was due to defects in the crystal lattice structures that formed when Zn⁺, which has a higher Shannon diameter, replaced Ni⁺, which has a smaller Shannon diameter. The present study's findings pave the way for producing nano-composites with improved properties by combining elements with large ionic diameters into a lattice comprising elements with small ionic diameters.

5. ACKNOWLEDGEMENTS

The authors would like to acknowledge that this research was conducted independently, without external funding or support.

6. REFERENCES

- 1. Ahamed, N. N. et al. (2024). Electro-chemical studies of Zn doped nickel oxide nanoparticles synthesized via solution combustion method using green and chemical fuels. *RSC advances*, 14(25), 17664–17674. https://doi.org/10.1039/D4RA01706D
- 2. Ahmed, A. A. A. et al. (2021). The influence of Zn and Mg doping on the structural and optical properties of NiO nano-structures for optoelectronic applications. *Results in Physics*, 22, 103938. https://doi.org/10.1016/j.rinp.2021.103938
- 3. Benhamida, S. et al. (2021). Structural, optical and dielectric properties of Zn-doped NiO thin films synthesized via sol-gel route. *Dig. J. Nanomater. Biostruct*, *16*, 433–442. https://chalcogen.ro/433_BenhamidaS.pdf.
- Raja, K. et al. (2014). Synthesis, structural and optical properties of ZnO and Nidoped ZnO hexagonal nanorods by co-precipitation method. Spectrochimica Acta Part A: Molecular and Biomolecular Spectroscopy, 120, 19–24. https://doi.org/10.1016/j.saa.2013.09.103
- 5. Yeşiltepe Özcelik, D. et al. (2022). Mixed oxides NiO/ZnO/Al₂O₃ synthesized in a single step via ultrasonic spray pyrolysis (USP) method. *Metals*, 12(1), 73. https://doi.org/10.3390/met12010073
- 6. Panigrahi, U. K. et al. (2020). Zn doping induced enhancement of multifunctional properties in NiO nanoparticles. *J. Alloys Compd.*, 833, 155050. https://doi.org/10.1016/j.jallcom.2020.155050
- 7. Ismail, H. et al. (2022). Compatibility of concentrated NaOH as a precipitation agent in the synthesis of maghemite (γ-Fe₂O₃) nanoparticles via co-precipitation method. *J. Phys. Sci.*, 33(2), 61–75. https://doi.org/10.21315/jps2022.33.2.4
- 8. Rambu, A. P. et al. (2013). Study on Ni-doped ZnO films as gas sensors. *Appl. Surf. Sci.*, 280, 598–604. https://doi.org/10.1016/j.apsusc.2013.05.033
- 9. Hameed, I. A. et al. (2023). Characteristics and biological applications of green nickel Oxide synthesised by *Hibiscus Sabdariffa* flowers. *Mater. Sci. Forum*, 1084, 31–40. https://doi.org/10.4028/p-q91860
- 10. Fabbiyola, S. et al. (2017). Optical and magnetic properties of Ni-doped ZnO nanoparticles. *J. Alloys Compd.*, 694, 522–531. https://doi.org/10.1016/j.jallcom.2016.10.022
- 11. Srinivasulu, T. et al. (2017). Synthesis and characterization of Fe-doped ZnO thin films deposited by chemical spray pyrolysis. *Mod. Electron. Mater.*, 3(2), 76–85. https://doi.org/10.1016/j.moem.2017.07.001
- 12. Abed, M. A. et al. (2021). Synthesis and characterization of chemically sprayed Cu₂FeSnS₄ (CFTS) thin films: The effect of substrate temperature. *Mater. Sci. Forum*, 1039, 434–441. https://doi.org/10.4028/www.scientific.net/MSF.1039.434
- 13. Siddique, M. N. et al. (2018). Enhanced electrical and thermal properties of pure and Ni substituted ZnO nanoparticles. *Nano-Struct. Nano-Objects* 16, 156–166. https://doi.org/10.1016/j.nanoso.2018.06.001
- 14. Abed, M. A. et al. (2023). Physical properties and antibacterial activity of green-iron oxide nanoparticles synthesize with chia seeds. *Chem. Data Collect.*, 44, 101013. https://doi.org/10.1016/j.cdc.2023.101013

- Abdel Maksoud, M. I. A. et al. (2020). Influence of Mg²⁺ substitution on structural, optical, magnetic, and antimicrobial properties of Mn–Zn ferrite nanoparticles. J. Mater. Sci.: Mater. Electron., 31, 2598–2616. https://doi.org/10.1007/s10854-019-02799-4
- Ali, D. et al. (2019). Synthesis and characterization of sol-gel derived La and Sm doped ZnO thin films: A solar light photo catalyst for methylene blue. *Thin Solid Films*, 679, 86–98. https://doi.org/10.1016/j.tsf.2019.04.017
- 17. Zeid, E. F. A. et al. (2019). The effect of CdO content on the crystal structure, surface morphology, optical properties and photocatalytic efficiency of p-NiO/n-CdO nanocomposite. *Results Phys.*, 12, 562–570. https://doi.org/10.1016/j.rinp.2018.12.009
- 18. Alsaad, A. M. et al. (2020). Measurement and ab initio investigation of structural, electronic, optical, and mechanical properties of sputtered aluminum nitride thin films. *Front. Phys.*, 8, 115. https://doi.org/10.3389/fphy.2020.00115
- 19. Mamat, M. H. et al. (2020). Synthesis, structural and optical properties of mesostructured, X-doped NiO (x = Zn, Sn, Fe) nanoflake network films. *Mater. Res. Bull.*, 127, 110860. https://doi.org/10.1016/j.materresbull.2020.110860
- 20. Rathika, G. et al. (2024). Surface and quantum chemical parameters of nickel oxide nanostructures suited for ultraviolet-assisted cationic dye degradation. *Kuwait J. Sci.*, 51(2), 100200. https://doi.org/10.1016/j.kjs.2024.100200
- Panigrahi, U. K. et al. (2019). Structural, optical and magnetic properties of Ni_{1-x} Zn _x O/Ni nanocomposite. SN Applied Sciences, 1, 1–13. https://doi.org/10.1007/s42452-019-0461-0
- 22. Vara, J. A. et al. (2019). The catalytic activity of transition metal oxide nanoparticles on thermal decomposition of ammonium perchlorate. *Def. Technol.*, 15(4), 629–635. https://doi.org/10.1016/j.dt.2019.04.002
- 23. Aalami, Z. et al. (2024). Synthesis, characterization, and photocatalytic activities of green sol-gel ZnO nanoparticles using *Abelmoschus esculentus* and *Salvia officinalis*: A comparative study versus co-precipitation-synthesized nanoparticles. *Heliyon*, 10(2). https://doi.org/10.1016/j.heliyon.2024.e24212
- 24. Yedurkar, S. et al. (2016). Biosynthesis of zinc oxide nanoparticles using ixora coccinea leaf extract—a green approach. *Open J. Synth. Theory Appl.*, 5(1), 1–14. https://doi.org/10.4236/ojsta.2016.51001
- 25. Dulta, K. et al. (2022). Ecofriendly synthesis of zinc oxide nanoparticles by Carica papaya leaf extract and their applications. *J. Clust. Sci.*, 1–15. https://doi.org/10.1007/s10876-020-01962-w
- Mane, P. et al. (2021). Biogenic synthesis of ZnO nanoparticles from Parthenium histerophorus extract and its catalytic activity for building bioactive polyhydroquinolines. *Res. Chem. Intermed.*, 47, 1743–1758. https://doi.org/10.1007/ s11164-020-04365-8

- 27. da Silva-Neto, M. L. et al. (2019). UV random laser emission from flexible ZnO-Agenriched electrospun cellulose acetate fiber matrix. *Sci. Rep.*, 9(1), 11765. https://doi.org/10.1038/s41598-019-48056-w
- 28. Kumar, C. R. et al. (2020). Photocatalytic, nitrite sensing and antibacterial studies of facile bio-synthesized nickel oxide nanoparticles. *J. Sci.: Adv. Mater. Devices*, 5(1), 48–55. https://doi.org/10.1016/j.jsamd.2020.02.002
- 29. Murthy, K. R. S. et al. (2021). Zinc oxide nanostructured material for sensor application. *J. Biotechnol. Bioeng.*, 5, 25–29. https://doi.org/10.22259/2637-5362.0501004
- Haq, S. et al. (2021). Phytogenic synthesis and characterization of NiO-ZnO nanocomposite for the photodegradation of brilliant green and 4-Nitrophenol. *J. Chem.*, 2021(1), 3475036. https://doi.org/10.1155/2021/3475036
- 31. Elkamel, I. B. et al. (2018). High responsivity and 1/f noise of an ultraviolet photodetector based on Ni doped ZnO nanoparticles. *RSC Adv.*, 8(56), 32333–32343. https://doi.org/10.1039/C8RA05567J
- 32. Hassan, I. (2019). Ameliorative effect of zinc oxide nanoparticles against potassium bromate-mediated toxicity in Swiss albino rats. *Environ. Sci. Pollut. Res.*, 26, 9966–9980. https://doi.org/10.1007/s11356-019-04443-4
- 33. Ali, F. M. et al. (2012). Influence of annealing on structural, morphological and optical properties of Cd_x Zn_{1-x} O nanopowder prepared by Co-precipitation method. *Mater. Sci.-Pol.*, 30, 248–253. https://doi.org/10.2478/s13536-012-0027-y
- 34. Rini, A. S. et al. (2023). Synthesis and characterisation of ZnO/Ag nanocomposites prepared via green method using pineapple peel extract for photocatalytic enhancement in degrading methylene blue dye solutions. *J. Phys. Sci.*, 34(2), 59–73. https://doi.org/10.21315/jps2023.34.2.5
- 35. Patel, M. et al. (2016). Nanostructured SnS with inherent anisotropic optical properties for high photoactivity. *Nanoscale*, 8(4), 2293–2303. https://doi.org/10.1039/C5NR06731F
- e Silva, R. L. et al. (2019). Functional properties of donor-and acceptor-co-doped high dielectric constant zinc oxide ceramics. *Phys. Chem. Chem. Phys.*, 21(18), 9456–9464. https://doi.org/10.1039/C9CP01140D
- 37. Li, W. et al. (2020). Defects in complex oxide thin films for electronics and energy applications: Challenges and opportunities. *Mater. Horiz.*, 7(11), 2832–2859. https://doi.org/10.1039/D0MH00899K